# Orthogonal-Sided Polished Microstructured Optical Fiber-Based SPR Sensor for Simultaneous Measurement of Temperature and Refractive Index

Nannan Luan, Donglian Hou, Xianxing Ji, Wandi Zhang, Yaoyao Qi, Li Song, and Jianfei Liu

***Abstract*—We propose a concept of orthogonal-side polished microstructured optical fiber (MOF)-based surface plasmon resonance (SPR) sensor to implement the simultaneous sensing for two parameters. Two feasible structures, L-shaped MOF based and rectangular MOF based SPR sensors are investigated theoretically, which can support *x*- and *y*-polarized resonance peaks that can be used to measure and separate variations of the temperature and refractive index (RI). Our results show that the temperature coefficients ($K_{Tx}$ and $K_{Ty}$) are 8 pm/°C and 6 pm/°C, and the RI coefficients ($K_{nx}$ and $K_{ny}$) are 1470 nm/RIU and 1570 nm/RIU, for the L-shaped MOF-SPR sensor, while the $K_{Tx}$ and the $K_{Ty}$ are 10 pm/°C and 8 pm/°C, the $K_{nx}$ and $K_{ny}$ are 1460 nm/RIU and 1500 nm/RIU, for the rectangular MOF-based SPR sensor. Moreover, these coefficients can be further improved by choosing the appropriate structure parameters. The proposed SPR sensors with the advantages of simultaneously measuring two parameters and no need to be filled with the sensing media are expected to be more competitive in the MOF-based SPR sensor field.**

***Index Terms*—Microstructured optical fiber, optical fiber sensor, refractive index, surface plasmon resonance, temperature.**

## I. Introduction

RECENTLY, microstructured optical fiber (MOF) based surface plasmon resonance (SPR) sensors have attracted more attention because of their advantages of flexible structure design and adjustable optical properties [1]–[12]. Compared with the traditional fiber based SPR sensors, one of the main advantages of the MOF-based SPR sensors is that it can boost the phase matching problems, and thus effectively tuning the resonance wavelength and improving the sensing performance [12]–[16]. In the early development of the MOF-based SPR sensors, to implement SPR sensing for liquid samples, the holes of the MOFs need to be coated with the metal films or placed with wires, and then filled with the samples [10], [13]–[18]. Due to the high sensitivity of the SPR on the refractive index (RI) of the liquid samples, the MOF-based SPR sensors also can realize temperature sensing by filling the holes with sensing mediums with high temperature coefficient instead of liquid samples [19]–[21]. However, the manufacturing operations in these MOF-based SPR sensors yield two main disadvantages.

The first disadvantage is the complex processing for the sensor fabrication. In the most MOF-based SPR sensors [10], [13]–[18], to achieve SPR, the several-micron-size holes of the used MOFs must be deposited with the metal layers by special methods, such as electroless plating techniques or chemical vapor deposition techniques [13]. Although, the metal layers can be replaced by the metal wires [18], it is also hard to operate in such small holes. Moreover, the liquid samples or sensing mediums also need to be filled into these holes. These complicated operations in sensor fabrication are very difficult to control, and thus reducing the convenience of the sensor application.

The second disadvantage of those MOF-based SPR sensors is that the sensors can only determine and measure one parameter at one time [10]–[21]. As mentioned above, the MOF-based SPR sensor is very sensitivity to the change of RI of the materials on metal surface, theoretically, any factor that can affect the RI of the materials can be detected. However, it is difficult to distinguish which factors that cause the RI changes, and therefore those MOF-based SPR sensors can only detect one factor at a particular circumstance. For example, the MOF-based SPR sensors can only measure the RI changes by filling the air holes with samples [11]–[18], or the temperature changes by filling the air holes with the sensing mediums whose RI is easy affected by the temperature changes [19]–[21].

Currently, the open-style MOFs, including the exposed core MOFs and the side polished MOFs, have been used as a substitute to fabricate the SPR sensors for RI or temperature sensing [22]–[37]. These novel open-style structures can be easy to be metallized for SPR, such as deposited with the metal layers or placed with the metal wires, and therefore they not only simplify the sensor fabrication but also obtain the function for real-time sensing which is hard to realize by using the conventional MOFs. In addition, by arranging two vertical sensing channels in one open-style MOF-based SPR sensors, they can measure two parameters (RI and temperature) simultaneously [38]–[41]. However, for temperature sensing in those design, the sensing

Manuscript received January 10, 2022; revised February 28, 2022; accepted March 19, 2022. Date of publication March 28, 2022; date of current version April 27, 2022. This work was supported in part by the Natural Science Foundation of Hebei Province under Grants F2019202294, F2019202252, and F2019202467. *(Corresponding author: Li Song.)*

The authors are with the School of Electronic and Information Engineering, Hebei University of Technology, Tianjin 300401, China (e-mail: nannanluan@gmail.com; 201921902013@stu.hebut.edu.cn; 202021902017@stu.hebut.edu.cn; 202131903016@stu.hebut.edu.cn; qiyao@hebut.edu.cn; songli@hebut.edu.cn; jfliu@hebut.edu.cn).

Digital Object Identifier 10.1109/JPHOT.2022.3161468

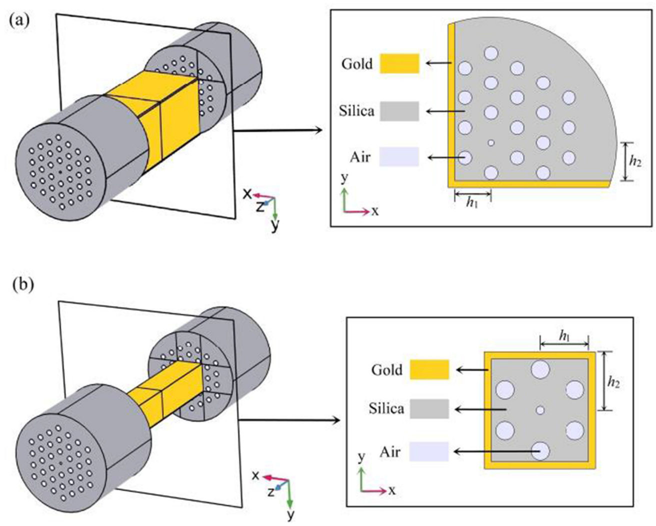


Fig. 1. Schematic diagram of the L-shaped (a) and rectangular (b) MOF-SPR sensors in 3D view and cross-section view.

channel is the air hole which is also needed to be coated with the metal layer and filled with the sensing medium inevitably [38]–[41].

To overcome the above problems, in this work, we propose two designs of the orthogonal-side polished MOF-based SPR sensors for simultaneous sensing of RI and temperature. The polished planes in these MOFs can be easily coated with the gold layers and in contact with the sample for the RI sensing. For the temperature sensing, they mainly depend on the changes of the properties of the fiber and of the gold layer caused by the variations of the temperature, and therefore do not need extra sensing medium. The proposed structures can support *x*- and *y*-polarized resonance peaks that can present strong dependency to the changing of the sample RI and temperature. By monitoring the changes of the two polarized resonance peaks, the changes of the sample RI and temperature can be separated, and thus determined simultaneously.

## II. Structure and Method

In order to create the *x*- and *y*- polarized resonance peaks simultaneously for the different characteristics of sample RI and temperature, we propose two feasible orthogonal-side polished MOFs to fabricate the SPR sensor, as shown in Fig. 1. In the first MOF, see Fig. 1(a), the fiber is polished two sides to form the L-shaped cross-section. In the second MOF, see Fig. 1(b), the fiber is polished four sides to form the rectangular cross-section. These structures could be fabricated accurately at a 3D mechanical platform that can move along the X, Y, and Z directions to operate the polishing position, length, and depth [29]. The polished planes of the two MOFs can be easy coated with the gold layer uniformly. Moreover, to lower the RI of the core mode to facilitate the phase matching problem [12]–[16], [25], [26], we also introduce a small air hole into the core center of the two fiber. In order to investigate and contrast their sensing performance, the two sensors have the same structure parameters. As shown in Fig. 1, the lattice pitch is $\Lambda = 2$ μm and the diameter of the cladding holes is $0.45\Lambda$. The polishing depths in the horizontal and vertical directions are $h_1 = 1.2\Lambda$ and $h_2 = 1.25\Lambda$, respectively. The thickness of the gold layer is $m = 40$ nm, and the diameter of the central hole is $d_c = 0.1\Lambda$.

We employ the COMSOL Multiphysics software with the finite element method (FEM) to investigate the core mode and surface plasmon polariton (SPP) mode of the sensors. A perfect match layers with 2 μm thickness boundary is used to matching the outmost layer, and the triangular normal mesh is adopted to discretize the computation area. In the FEM, the RI of the air is set to be 1 and assumed independent with the variation of the temperature. The material dispersion of the silica is given as [20], [42]

$$n^2(\lambda, T) = (1.31552 + 0.690754 \times 10^{-5}T) + \frac{(0.788404 + 0.235835 \times 10^{-4}T)\lambda^2}{\lambda^2 - (0.0110199 + 0.584758 \times 10^{-6}T)} + \frac{(0.91316 + 0.548368 \times 10^{-6}T)\lambda^2}{\lambda^2 - 100} \tag{1}$$

where $\lambda$ is the wavelength in microns and $T$ is the temperature in degrees Celsius. The permittivity of the gold $\varepsilon(\omega)$ can be calculated by the Drude formula [20]

$$\varepsilon(\omega, T) = \varepsilon_1 + i\varepsilon_2 = \varepsilon_\infty - \frac{\omega_p(T)^2}{\omega(\omega + i\omega_c(T))} \tag{2}$$

where the $\varepsilon_\infty$ is the permittivity in high frequency, the $\omega_p(T)$ and the $\omega_c(T)$ represent the plasma frequency and the collision frequency, respectively. The $\omega_p(T)$ is expressed as [20]

$$\omega_p(T) = \omega_{p0} \times \exp\left(-\frac{T - T_0}{2} \times \alpha_V(T_0)\right) \tag{3}$$

Here, the $\omega_{p0}$ is the plasma frequency at room temperature $T_0 = 298.15$K. The $\alpha_V$ is the thermal volume expansion coefficient of gold. The $\omega_c(T)$ includes two factors, and can be calculated by the equation [20], [43]

$$\omega_c(T) = \omega_{ce}(T) + \omega_{cp}(T) \tag{4}$$

The $\omega_{ce}(T)$ is electron-electron scattering frequency which can be represented by the Lawrence model [20], [44]

$$\omega_{ce}(T) = \frac{1}{6}\pi^4 \frac{\Gamma\Delta}{hE_F}\left[(k_B T)^2 + \left(\frac{h\omega}{4\pi^2}\right)^2\right] \tag{5}$$

where the $\Gamma$ and the $\Delta$ are defined in Ref. [20], [43], the $h$ and the $k_B$ are Planck constant and Boltzmann constant respectively. And the $\omega_{cp}(T)$ is phonon-electron scattering that can be given by [20], [44]

$$\omega_{cp}(T) = \omega_0\left[\frac{2}{5} + 4\left(\frac{T}{T_D}\right)^5 \int_0^{T_D/T} \frac{z^4 dz}{e^z - 1}\right] \tag{6}$$

Here the $\omega_0$ is a constant that can be determined by calculated the (2), (4) and (5) at $T_0 = 298.15$K [20]. The $T_D$ is the Debye temperature in degrees Kelvin [20].

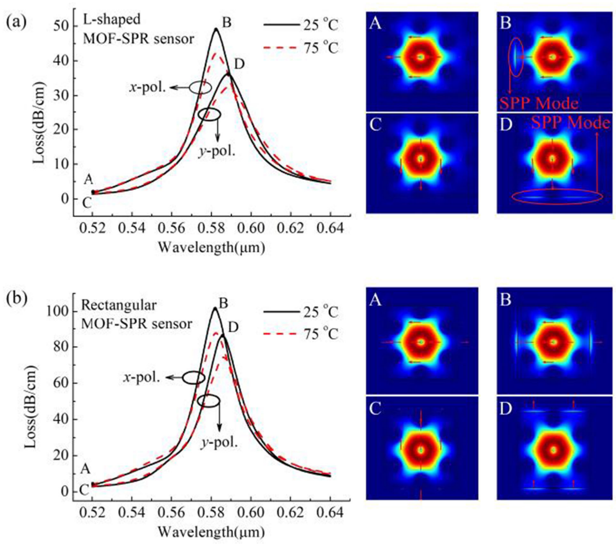


Fig. 2. The x- and y-polarized loss spectra of the L-shaped (a) and rectangular (b) MOF-SPR sensors with varying temperature from 25 °C to 75 °C. Insets A-D show the electric field distribution of the relevant core modes.

Besides, the thickness of the gold layer $m(T)$ variation with the temperature changing can be evaluated by [20], [44], [45]

$$m(T) = m_0 \left[1 + \alpha_L \frac{1+\mu}{1-\mu}(T - T_0)\right] \tag{7}$$

where $m_0$ is the thickness of the gold layer at $T_0 = 298.15$K, the $\alpha_L$ and the $\mu$ are the linear thermal expansion coefficient and the Poisson number of the metal, respectively [20], [44], [45].

## III. Numerical Result and Analysis

Fig. 2 shows the x- and y-polarized loss spectra of the L-shaped and rectangular MOF-SPR sensors with temperature changing from 25 °C to 75 °C, when the RI of the sample is 1.33. The insets in Fig. 2 are the electric field distribution of the core modes corresponding to the particular wavelengths in the Fig. 2(a) and (b) respectively, which clearly show the energy transfer between the core modes and SPP modes. Take the x-polarized loss spectrum of the core mode in L-shaped MOF-SPR sensor at $T = 25$ °C for instance, at the unresonance wavelength A, the energy distributes in the core region, as the inset A shown in Fig. 2(a), and part of it transfers to the SPP mode at the resonance wavelength B, as seen from the inset B in which the small bright region on the left side of the center is the energy of the SPP mode. This process of the energy transfer is similar to what happens in the rectangular MOF-SPR sensor. However, there is an important difference in energy transfer between the two structure: the part of the energy of the core mode transfer to the SPP mode at one side in the L-shaped MOF-SPR sensor, while that transfer to the SPP mode at two sides in the rectangular MOF-SPR sensor. This difference leads to a prime result is that the mode loss at the resonance wavelength in the rectangular MOF-SPR sensor is higher than that in the L-shaped MOF-SPR sensor, and thus contributing to a narrower resonance spectral width which can offer a better sensing resolution and

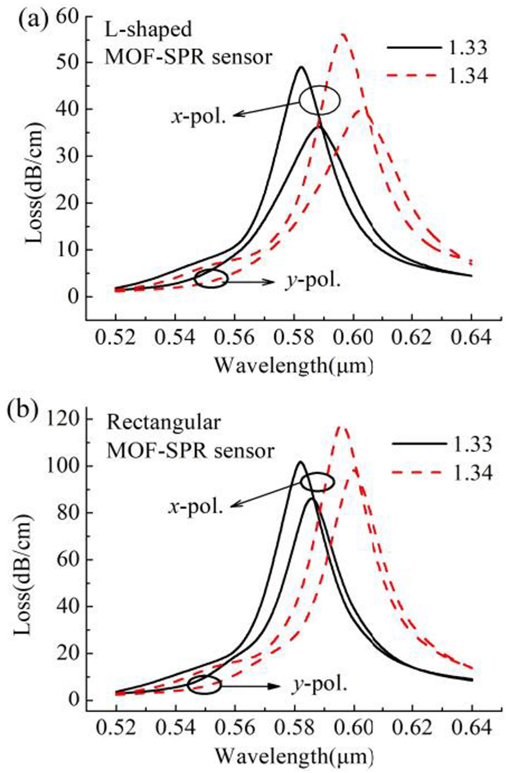


Fig. 3. The x- and y-polarized loss spectra of the L-shaped (a) and rectangular (b) MOF-SPR sensors with varying RI from 1.33 to 1.34.

SNR (signal to noise ratio). From the Fig. 2, it can be seen clearly that both of the x- and y-polarized resonance peaks shift to longer wavelength as the temperature variation from 25°C to 75°C. While they also move to longer wavelength as the RI increasing as seen from Fig. 3 that presents the x- and y-polarized loss spectra of L-shaped and rectangular MOF-SPR sensors with RI of the sample changing from 1.33 to 1.34 when the temperature is 25°C.

To simultaneously measure both variations of temperature ($\Delta T$) and RI ($\Delta n$) and distinguish them by monitoring the shifts of the x- and y-polarized peaks ($\Delta\lambda_x$ and $\Delta\lambda_y$), we employ the following equation [44], [45]

$$\begin{bmatrix} \Delta\lambda_x \\ \Delta\lambda_y \end{bmatrix} = \begin{bmatrix} K_{Tx} & K_{nx} \\ K_{Ty} & K_{ny} \end{bmatrix} \cdot \begin{bmatrix} \Delta T \\ \Delta n \end{bmatrix}. \tag{8}$$

Here $K_{Tx}$ and $K_{Ty}$ are the temperature coefficients of the x- and y-polarized peaks respectively, and $K_{nx}$ and $K_{ny}$ are the RI coefficients of the x- and y-polarized peaks respectively. Therefore, the $\Delta T$ and $\Delta n$ can expressed as

$$\begin{bmatrix} \Delta T \\ \Delta n \end{bmatrix} = \begin{bmatrix} K_{Tx} & K_{nx} \\ K_{Ty} & K_{ny} \end{bmatrix}^{-1} \cdot \begin{bmatrix} \Delta\lambda_x \\ \Delta\lambda_y \end{bmatrix}. \tag{9}$$

Here we assume that the shifts of the peaks are linear variations for the changes of RI and temperature in the computing range. Therefore, according to the data from the Figs. 2 and 3, we can calculate that the $K_{Tx}$ and the $K_{Ty}$ are both 6 pm/°C, and the $K_{nx}$ and $K_{ny}$ are 1390 nm/RIU and 1480 nm/RIU respectively, for the L-shaped MOF-SPR sensor. The $K_{Tx}$ and the $K_{Ty}$ are

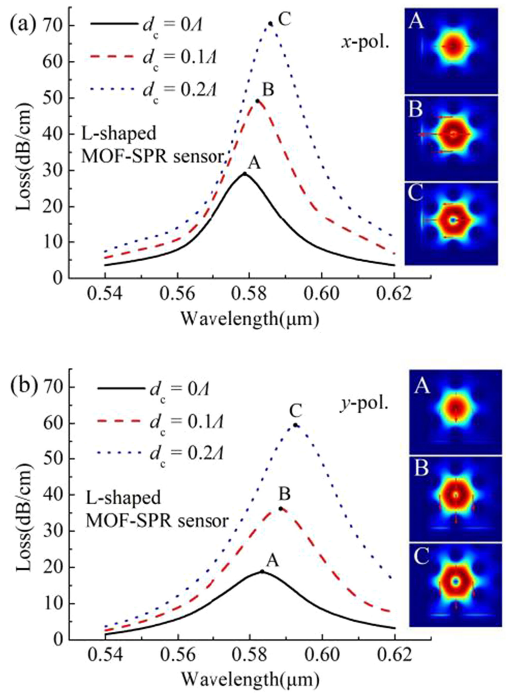


Fig. 4. The *x*-polarized (a) and *y*-polarized (b) loss spectra of the L-shaped MOF-SPR sensor with the three different values of $d_c = 0\Lambda$, $0.1\Lambda$ and $0.2\Lambda$. Insets A-C show the electric field distribution of the relevant core modes at resonance wavelengths.

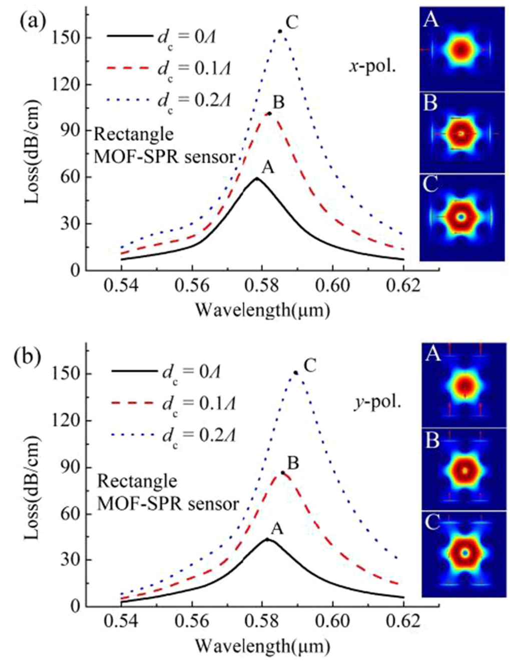


Fig. 5. The *x*-polarized (a) and *y*-polarized (b) loss spectra of the rectangular MOF-SPR sensor with the three different values of $d_c = 0\Lambda$, $0.1\Lambda$ and $0.2\Lambda$. Insets A-C show the electric field distribution of the relevant core modes at resonance wavelengths.

10 pm/°C and 8 pm/°C respectively, and the $K_{nx}$ and $K_{ny}$ are 1400 nm/RIU and 1430 nm/RIU respectively, for the rectangular MOF-SPR sensor. According to the (9), the $\Delta T$ and $\Delta n$ can be determined as

$$\begin{bmatrix} \Delta T \\ \Delta n \end{bmatrix} = \begin{bmatrix} 2740.740741 & -2574.074074 \\ -0.011111 & 0.011111 \end{bmatrix} \cdot \begin{bmatrix} \Delta\lambda_x \\ \Delta\lambda_y \end{bmatrix} \quad (10)$$

for L-shaped MOF-SPR sensor, and

$$\begin{bmatrix} \Delta T \\ \Delta n \end{bmatrix} = \begin{bmatrix} 461.290323 & -451.612903 \\ -0.002581 & 0.003226 \end{bmatrix} \cdot \begin{bmatrix} \Delta\lambda_x \\ \Delta\lambda_y \end{bmatrix} \quad (11)$$

for the rectangular MOF-SPR sensor.

## IV. Discussion

### A. Effects of the Sizes of Center Hole Changes on Sensing Performance

In these two sensors, an air hole is introduced into the fiber core to lower the effective RI ($n_{\mathrm{eff}}$) of a core mode, which is a common way to facilitate the phase matching and improve the sensing performance [12]–[16], [25], [26]. Figs. 4 and 5 exemplarily depict the *x*- and *y*-polarized loss spectra of the L-shaped and rectangular MOF-SPR sensors for various diameters of the central hole $d_c = 0\Lambda$, $0.1\Lambda$ and $0.2\Lambda$ when the temperature is 25 °C and the RI of the sample is 1.33. From the Figs. 4 and 5, it can be seen that the main effect of increasing $d_c$ is an overall increase in the resonance wavelengths and the peak losses. The larger $d_c$ can reduce the $n_{\mathrm{eff}}$ of the core modes effectively, and thus leading to the movement of a resonance peak toward longer wavelengths [12]–[16], [25], [26]. Another consequence of the larger $d_c$ is expulsion of the modal field from the centre of the core area to the metallic interface, as seen from insets A-C in the Figs. 4 and 5, which enhances the resonance and resulting in higher peak losses.

TABLE I
Summary of Performances of the L-Shaped and Rectangular MOF-SPR Sensors With Various Diameters of the Central Hole

| $d_c/\Lambda$ | L-shaped MOF-SPR sensor | | | | Rectangular MOF-SPR sensor | | | |
|---|---|---|---|---|---|---|---|---|
| | $K_{Tx}$ (pm/°C) | $K_{Ty}$ (pm/°C) | $K_{nx}$ (nm/RIU) | $K_{ny}$ (nm/RIU) | $K_{Tx}$ (pm/°C) | $K_{Ty}$ (pm/°C) | $K_{nx}$ (nm/RIU) | $K_{ny}$ (nm/RIU) |
| 0 | 10 | 6 | 1340 | 1400 | 8 | 8 | 1320 | 1350 |
| 0.1 | 6 | 6 | 1390 | 1480 | 10 | 8 | 1400 | 1430 |
| 0.2 | 8 | 6 | 1470 | 1570 | 10 | 8 | 1460 | 1500 |

Table I summarizes the performances of the L-shaped and the rectangular MOF-SPR sensors in terms of temperature coefficients ($K_{Tx}$ and $K_{Ty}$) and RI coefficients ($K_{nx}$ and $K_{ny}$) when the $d_c$ is $0\Lambda$, $0.1\Lambda$ and $0.2\Lambda$, respectively. For the temperature sensing, the temperature coefficient appears a little irregular behavior as $d_c$ changing, because it is effected by many complicated factors, such as thermal expansion effect, phonon-electron and electron-electron scatterings. While for the RI sensing, RI coefficient shows a growing tendency with the $d_c$ increasing, because the larger $d_c$ can lower the $n_{\mathrm{eff}}$ of a core mode, hence facilitating the phase matching between the core modes and the SPP modes, and resulting in a higher RI sensitivity [12]–[16], [25], [26].

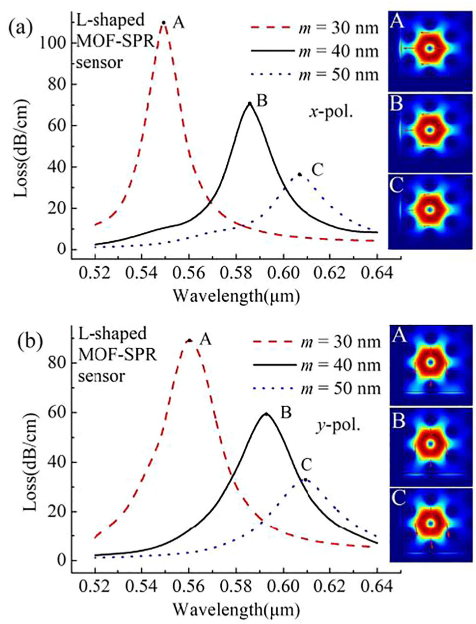


Fig. 6. The *x*-polarized (a) and *y*-polarized (b) loss spectra of the L-shaped MOF-SPR sensors with the three different values of $m = 30$ nm, 40 nm and 50 nm. Insets A-C show the electric field distribution of the relevant core modes at resonance wavelengths.

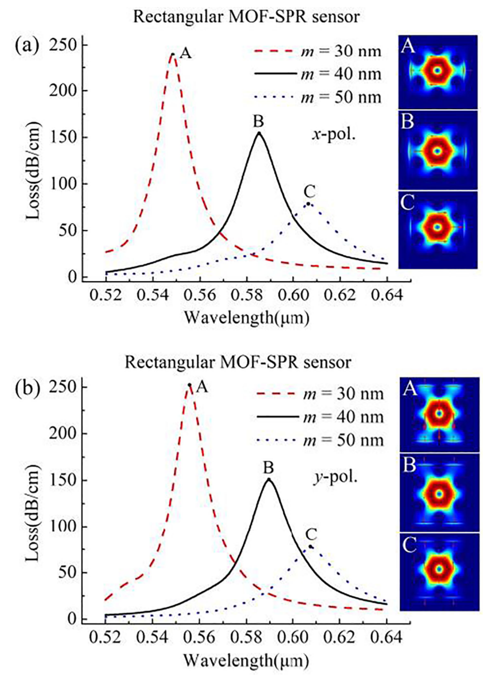


Fig. 7. The *x*-polarized (a) and *y*-polarized (b) loss spectra of the rectangular MOF-SPR sensors with the three different values of $m = 30$ nm, 40 nm and 50 nm. Insets A-C show the electric field distribution of the relevant core modes at resonance wavelengths.

### *B. Effects of the Thickness of the Gold Layer Change on Sensing Performance*

In the MOF-SPR sensors, the thickness of the metallic layer is an important parameter that can influence the SPR spectra and the sensor performances [12]–[16], [19]–[21], [26]–[28], [30], [34]–[36]. In Figs. 6 and 7, we exemplarily depict the loss spectra of the core modes for the two MOF designs of Fig. 1 with 30 nm, 40 nm and 50 nm thicknesses ($m$) of a gold layer when the $d_c$ is 0.2Λ, the temperature is 25 °C and the RI of the sample is 1.33. Generally, the mode loss of the resonance peak decreases with the $m$ increasing, and simultaneously, the wavelength of the resonance peak shifts toward longer wavelengths. This peak behavior is caused by the fact that the thicker gold layer can weaken the energy transfer from the core modes to the SPP modes, as seen from insets A-C in Figs. 6 and 7, and also increase the $n_{\text{eff}}$ of the SPP modes at the metal dielectric interface, and thus requiring longer wavelength to match the phases of the core modes and SPP modes [12]–[16], [19]–[21], [26]–[28], [30], [34]–[36].

The sensing performances of the L-shaped and Rectangular MOF-SPR sensors caused by the various $m$ are summarized in Table II. As shown, in the both structures, the temperature coefficients still appear a little irregular behavior with the $m$ changing, while the RI coefficients are increasing as the $m$ increasing. Moreover, coating with thinner gold layer can also support a narrower resonance spectral width in the both MOF-SPR sensors as shown in Figs. 6 and 7. In the aspect of the RI sensing, the variations of the resonance peaks and the sensing performances caused by the $m$ changing in the two SPR sensors are also consistent with that in the others MOF-SPR sensors [12]–[16], [19]–[21], [26]–[28], [30], [34]–[36].

TABLE II
SUMMARY OF PERFORMANCES OF THE L-SHAPED AND RECTANGULAR MOF-SPR SENSORS WITH VARIOUS THICKNESSES OF THE GOLD LAYER

| $m$(nm) | L-shaped MOF-SPR sensor | | | | Rectangular MOF-SPR sensor | | | |
|---|---|---|---|---|---|---|---|---|
| | $K_{Tx}$ | $K_{Ty}$ | $K_{nx}$ | $K_{ny}$ | $K_{Tx}$ | $K_{Ty}$ | $K_{nx}$ | $K_{ny}$ |
| | (pm/°C) | | (nm/RIU) | | (pm/°C) | | (nm/RIU) | |
| 30 | 8 | 8 | 1130 | 1260 | 8 | 10 | 1110 | 1230 |
| 40 | 8 | 6 | 1470 | 1570 | 10 | 8 | 1460 | 1500 |
| 50 | 6 | 10 | 1660 | 1680 | 10 | 8 | 1650 | 1600 |

### *C. Effects of the Polishing Depths Change on Sensing Performance*

In these two sensor structures, to construct two resonance peaks with orthogonal-polarization direction for simultaneous RI and temperature sensing, the way of orthogonal-side polishing is required, and the polishing depths ($h_1$ and $h_2$) are also the important parameters to determine the positions and intensities of the resonance peaks.

Figs. 8 and 9 exemplarily exhibit the loss spectra of the core modes for the two MOF designs with $h_1 = 1.2\Lambda$, $1.25\Lambda$ and $1.3\Lambda$ when the $d_c$ is 0.2Λ, the temperature is 25 °C and the RI of the sample is 1.33. As seen from the figures, the increase in the $h_1$ has a weak effect on the resonance peak of the *y*-polarized core mode, while the main effect of increase in the $h_1$ is the increase of wavelength of the resonance peak of the *x*-polarized core mode, as well as the decrease in the loss of the resonance peak. This effect is because the increasing $h_1$ actually increases the horizontal size of the core area, which can increase the $n_{\text{eff}}$ of the *x*-polarized core mode and thus leading to the resonance wavelength (phase-matching point) between the

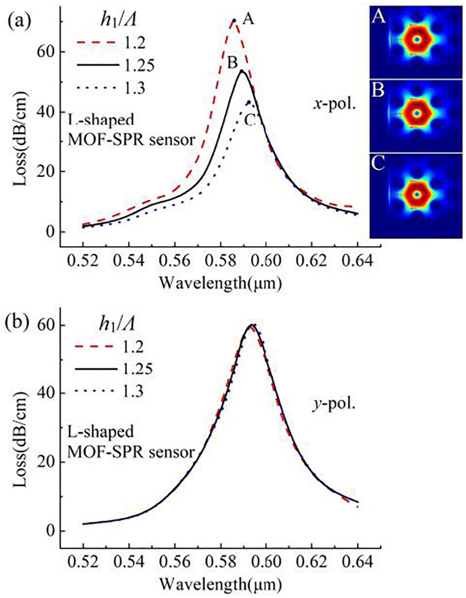


Fig. 8. The $x$-polarized (a) and $y$-polarized (b) loss spectra of the L-shaped MOF-SPR sensor with the three different values of $h_1 = 1.2\Lambda$, $1.25\Lambda$ and $1.3\Lambda$. Insets A-C show the $x$-polarized electric field distribution of the relevant core modes at resonance wavelengths.

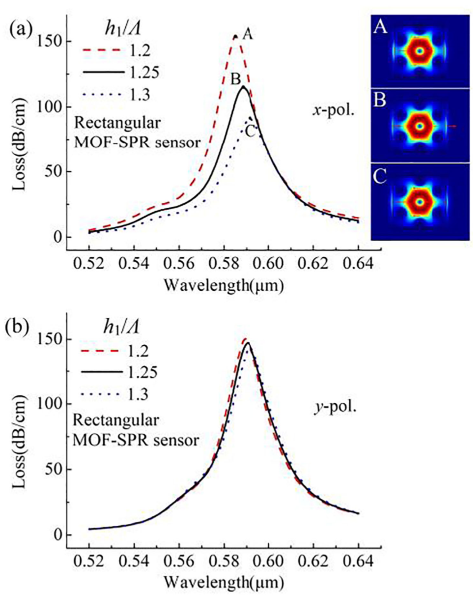


Fig. 9. The $x$-polarized (a) and $y$-polarized (b) loss spectra of the rectangular MOF-SPR sensor with the three different values of $h_1 = 1.2\Lambda$, $1.25\Lambda$ and $1.3\Lambda$. Insets A-C show the $x$-polarized electric field distribution of the relevant core modes at resonance wavelengths.

$x$-polarized core mode and SPP mode shift to longer wavelengths [12]–[16], [25], [26]. In addition, the increasing $h_1$ also increases the horizontal path distance between the core and the metal surface, which could weaken coupling intensity between the $x$-polarized core mode and SPP mode, as insets A-C shown in Figs. 8(a) and 9(a), and therefore resulting in a low loss of the $x$-polarized resonance peak.

Table III shows the effect of the various $h_1$ on the sensing performances of the L-shaped and Rectangular MOF-SPR

TABLE III
SUMMARY OF PERFORMANCES OF THE L-SHAPED AND RECTANGULAR MOF-SPR SENSORS WITH VARIOUS HORIZONTAL POLISHING DEPTH

| | L-shaped MOF-SPR sensor | | | | Rectangular MOF-SPR sensor | | | |
|---|---|---|---|---|---|---|---|---|
| $h_1/\Lambda$ | $K_{Tx}$ | $K_{Ty}$ | $K_{nx}$ | $K_{ny}$ | $K_{Tx}$ | $K_{Ty}$ | $K_{nx}$ | $K_{ny}$ |
| | (pm/°C) | | (nm/RIU) | | (pm/°C) | | (nm/RIU) | |
| 1.2 | 8 | 6 | 1470 | 1570 | 10 | 8 | 1460 | 1500 |
| 1.25 | 8 | 4 | 1550 | 1580 | 6 | 8 | 1530 | 1520 |
| 1.3 | 6 | 4 | 1610 | 1600 | 6 | 8 | 1590 | 1640 |

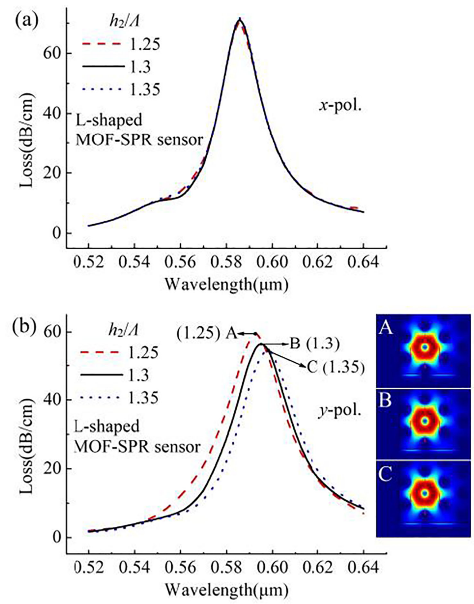


Fig. 10. The $x$-polarized (a) and $y$-polarized (b) loss spectra of the L-shaped MOF-SPR sensor with the three different values of the $h_2 = 1.25\Lambda$, $1.3\Lambda$ and $1.35\Lambda$. Insets A-C show the $y$-polarized electric field distribution of the relevant core modes at resonance wavelengths.

sensors. In the both structures, along with the $h_1$ increasing, the $K_{Tx}$ and $K_{Ty}$ are the downward trend, while the $K_{nx}$ and $K_{ny}$ show a general upward trend. Also note that the $K_{nx}$ increases more than the $K_{ny}$ for the same $h_1$ change because the $h_1$ increasing mainly increases the wavelength of the $x$-polarized resonance peak.

The effect of the change in $h_2$ on the loss spectra of the core modes for the two MOF designs with $h_2 = 1.25\Lambda$, $1.3\Lambda$ and $1.35\Lambda$ are shown in Figs. 10 and 11 when the $d_c$ is $0.2\Lambda$, the temperature is 25 °C and the RI of the sample is 1.33. Contrary to effect of changing $h_1$, the main effect of increasing $h_2$ are the increase in the wavelength and decrease in the loss of the $y$-polarized resonance peaks because the increasing $h_2$ actually increases the vertical size of the core area and the vertical path distance between the core and the metal surface.

The sensing performances of the L-shaped and Rectangular MOF-SPR sensors caused by the various $h_2$ are summarized in Table IV. As shown, in the both sensor structures, as the $h_2$ increasing, the $K_{Tx}$ and $K_{Ty}$ also show a downward trend, while the $K_{nx}$ and $K_{ny}$ show an overall upward trend. The increasing $h_2$ mainly increases the wavelength of the $y$-polarized resonance peak, and therefore the $K_{nx}$ increases less than the $K_{ny}$ for the same $h_2$ change which is also contrary to effect of changing $h_1$.

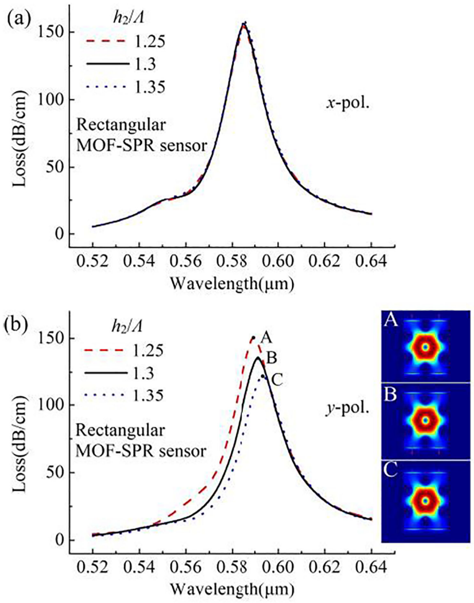


Fig. 11. The $x$-polarized (a) and $y$-polarized (b) loss spectra of the rectangular MOF-SPR sensor with the three different values of $h_2 = 1.25\Lambda$, $1.3\Lambda$ and $1.35\Lambda$. Insets A-C show the $y$-polarized electric field distribution of the relevant core modes at resonance wavelengths.

TABLE IV
SUMMARY OF PERFORMANCES OF THE L-SHAPED AND RECTANGULAR MOF-SPR SENSORS WITH VARIOUS VERTICAL POLISHING DEPTH

| | L-shaped MOF-SPR sensor | | | | Rectangular MOF-SPR sensor | | | |
|---|---|---|---|---|---|---|---|---|
| $h_2/\Lambda$ | $K_{Tx}$ | $K_{Ty}$ | $K_{nx}$ | $K_{ny}$ | $K_{Tx}$ | $K_{Ty}$ | $K_{nx}$ | $K_{ny}$ |
| | (pm/°C) | | (nm/RIU) | | (pm/°C) | | (nm/RIU) | |
| 1.25 | 8 | 6 | 1470 | 1570 | 10 | 8 | 1460 | 1500 |
| 1.3 | 8 | 6 | 1480 | 1630 | 8 | 8 | 1470 | 1540 |
| 1.35 | 8 | 4 | 1480 | 1700 | 8 | 8 | 1460 | 1590 |

## V. CONCLUSION

In conclusion, we investigate two orthogonal-side polished MOFs, L-shaped and rectangular MOFs, based SPR sensors for simultaneous RI and temperature sensing. The effects of the structure parameters, including the diameter of the central hole, the thickness of the gold layer and the polishing depths of horizontal and vertical directions, on the sensing performance of the two MOF-SPR sensors in terms of the SPR spectra, temperature coefficients and RI coefficients are analyzed. Numerical results show that the proposed sensors can support $x$- and $y$-polarized resonance peaks which can be used to measure simultaneously the variations of the temperature and the RI of the sample, and thus separate them. In addition, the proposed sensors also can solve the cross-sensitivity problem and facilitate the sensor calibration, and thus promoting more accurate measurements. The discussion and analysis of the two sensor structures can help them to be optimized to fit practical application and also could provide references for the designs of the D-shaped or double-side polished MOF-SPR sensors.

## REFERENCES

[1] A. A. Rifat *et al.*, "Photonic crystal fiber based plasmonic sensors," *Sensors Actuators B: Chem.*, vol. 243, pp. 311–325, 2017.
[2] A. K. Sharma, A. K. Pandey, and B. Kaur, "A review of advancements (2007–2017) in plasmonics-based optical fiber sensors," *Opt. Fiber Technol.*, vol. 43, pp. 20–34, 2018.
[3] C. Caucheteur, T. Guo, and J. Albert, "Review of plasmonic fiber optic biochemical sensors: Improving the limit of detection," *Anal. Bioanalytical Chem.*, vol. 407, no. 14, pp. 3883–3897, 2015.
[4] B. Lee, S. Roh, and J. Park, "Current status of micro- and nano-structured optical fiber sensors," *Opt. Fiber Technol.*, vol. 15, no. 3, pp. 209–221, 2009.
[5] E. Klantsataya, P. Jia, H. Ebendorff-Heidepriem, T. M. Monro, and A. Francois, "Plasmonic fiber optic refractometric sensors: From conventional architectures to recent design trends," *Sensors*, vol. 17, no. 1, 2016, Art. no. 12.
[6] P. Singh, "SPR biosensors: Historical perspectives and current challenges," *Sensors Actuators B: Chem.*, vol. 229, pp. 110–130, 2016.
[7] D. J. J. Hu and H. P. Ho, "Recent advances in plasmonic photonic crystal fibers: Design, fabrication and applications," *Adv. Opt. Photon.*, vol. 9, pp. 257–314, 2017.
[8] Y. Zhao, Z. Deng, and J. Li, "Photonic crystal fiber based surface plasmon resonance chemical sensors," *Sensors Actuators B: Chem.*, vol. 202, pp. 557–567, 2014.
[9] A. A. Rifat *et al.*, "Surface plasmon resonance photonic crystal fiber biosensor: A practical sensing approach," *IEEE Photon. Technol. Lett.*, vol. 27, no. 15, pp. 1628–1631, Aug. 2015.
[10] A. A. Rifat, G. A. Mahdiraji, D. M. Chow, Y. G. Shee, R. Ahmed, and F. R. M. Adikan, "Photonic crystal fiber-based surface plasmon resonance sensor with selective analyte channels and graphene-silver deposited core," *Sensors*, vol. 15, no. 5, pp. 11499–11510, 2015.
[11] M. A. Mollah, S. M. A. Razzak, A. K. Paul, and M. R. Hasan, "Microstructure optical fiber based plasmonic refractive index sensor," *Sens. Bio-Sens. Res.*, vol. 24, 2019, Art. no. 100286.
[12] A. Abbasiyan, M. Noori, M. Vakili, and N. Tourinezhad, "Analyte detection based on SPR in 12-fold quasi-periodic PCF," *Physica Scripta*, vol. 96, 2021, Art. no. 125506.
[13] A. Hassani and M. Skorobogatiy, "Design criteria for microstructured-optical-fiber-based surface-plasmon-resonance sensors," *J. Opt. Soc. Amer. B*, vol. 24, no. 6, pp. 1423–1429, 2007.
[14] A. Hassani and M. Skorobogatiy, "Design of the microstructured optical fiber-based surface plasmon resonance sensors with enhanced microfluidics," *Opt. Exp.*, vol. 14, no. 24, pp. 11616–11621, 2006.
[15] Y. Zhang *et al.*, "Microstructured fiber based plasmonic index sensor with optimized accuracy and calibration relation in large dynamic range," *Opt. Commun.*, vol. 284, no. 18, pp. 4161–4166, 2011.
[16] X. Yu *et al.*, "A selectively coated photonic crystal fiber based surface plasmon resonance sensor," *J. Opt.*, vol. 12, no. 1, 2010, Art. no. 015005.
[17] N. Luan and J. Yao, "A hollow-core photonic crystal fiber-based SPR sensor with large detection range," *IEEE Photon. J.*, vol. 9, no. 3, Jun. 2017, Art. no. 6802107.
[18] N. Luan and J. Yao, "High refractive index surface plasmon resonance sensor based on a silver wire filled hollow fiber," *IEEE Photon. J.*, vol. 8, no. 1, Feb. 2016, Art. no. 4800709.
[19] N. Luan, R. Wang, Y. Lu, and J. Yao, "Simulation of surface plasmon resonance temperature sensor based on liquid mixture-filling microstructured optical fiber," *Opt. Eng.*, vol. 53, 2014, Art. no. 067103.
[20] Y. Peng, J. Hou, Z. Huang, and Q. Lu, "Temperature sensor based on surface plasmon resonance within selectively coated photonic crystal fiber," *Appl. Opt.*, vol. 51, no. 26, pp. 6361–6367, 2012.
[21] N. Luan, R. Wang, Y. Lu, and J. Yao, "Surface plasmon resonance temperature sensor based on photonic crystal fibers randomly filled with silver nanowires," *Sensors*, vol. 14, pp. 16035–16045, 2014.
[22] N. Luan, R. Wang, W. Lv, and J. Yao, "Surface plasmon resonance sensor based on exposed-core microstructured optical fibers," *Electron. Lett.*, vol. 51, no. 9, pp. 714–715, 2015.
[23] E. Klantsataya, A. François, H. Ebendorff-Heidepriem, P. Hoffmann, and T. M. Monro, "Surface plasmon scattering in exposed core optical fiber for enhanced resolution refractive index sensing," *Sensors*, vol. 15, no. 10, pp. 25090–25102, 2015.
[24] N. Luan and J. Yao, "Surface plasmon resonance sensor based on exposed-core microstructured optical fiber placed with a silver wire," *IEEE Photon. J.*, vol. 8, no. 1, Feb. 2016, Art. no. 4800508.
[25] N. Luan, H. Han, L. Zhao, J. Liu, and J. Yao, "Opening up dual-core microstructured optical fiber-based plasmonic sensor with large detection range and linear sensitivity," *Opt. Mater. Exp.*, vol. 9, no. 2, pp. 819–825, 2019.
[26] N. Luan, R. Wang, W. Lv, and J. Yao, "Surface plasmon resonance sensor based on D-shaped microstructured optical fiber with hollow core," *Opt. Exp.*, vol. 23, no. 7, pp. 8576–8582, 2015.

[27] J. N. Dash and R. Jha, “Highly sensitive d shaped PCF sensor based on SPR for near IR,” *Opt. Quantum Electron.*, vol. 48, no. 2, 2016, Art. no. 137.

[28] M. N. Sakib *et al.*, “High performance dual core D-shape PCF-SPR sensor modeling employing gold coat,” *Results Phys.*, vol. 15, 2019, Art. no. 102788.

[29] T. Wu *et al.*, “Surface plasmon resonance biosensor based on gold-coated side-polished hexagonal structure photonic crystal fiber,” *Opt. Exp.*, vol. 25, no. 17, pp. 20313–20322, 2015.

[30] J. N. Dash and R. Jha, “On the performance of graphene-based D-shaped photonic crystal fibre biosensor using surface plasmon resonance,” *Plasmonics*, vol. 10, no. 5, pp. 1123–1131, 2015.

[31] M. P. Cardoso *et al.*, “Multi-plasmonic resonance based sensor for the characterization of optical dispersion using a D-shaped photonic crystal fiber,” *IEEE Instrum. Meas. Mag.*, vol. 24, no. 5, pp. 63–68, Aug. 2021.

[32] N. Luan, L. Zhao, Y. Lian, and S. Lou, “A high refractive index plasmonic sensor based on D-shaped photonic crystal fiber with laterally accessible hollow-core,” *IEEE Photon. J.*, vol. 10, no. 5, Oct. 2018, Art. no. 6803707.

[33] J. N. Dash and R. Jha, “Highly sensitive side-polished birefringent PCF-based SPR sensor in near IR,” *Plasmonics*, vol. 11, no. 6, pp. 1505–1509, 2016.

[34] D. Hou *et al.*, “Surface plasmon resonance sensor based on double-sided polished microstructured optical fiber with hollow core,” *IEEE Photon. J.*, vol. 13, no. 4, Aug. 2021, Art. no. 6800408.

[35] H. Han *et al.*, “A large detection-range plasmonic sensor based on an H-shaped photonic crystal fiber,” *Sensors*, vol. 20, no. 4, 2020, Art. no. 1009.

[36] H. Han *et al.*, “Surface plasmon resonance sensor based on dual-side polished microstructured optical fiber with dual-core,” *Sensors*, vol. 20, no. 14, 2020, Art. no. 3911.

[37] L. Zhao, H. Han, N. Luan, J. Liu, L. Song, and Y. Hu, “A temperature plasmonic sensor based on a side opening hollow fiber filled with high refractive index sensing medium,” *Sensors*, vol. 19, no. 17, 2019, Art. no. 3730.

[38] L. Zhao, H. Han, Y. Lian, N. Luan, and J. Liu, “Theoretical analysis of all-solid D-type photonic crystal fiber based plasmonic sensor for refractive index and temperature sensing,” *Opt. Fiber Technol.*, vol. 50, pp. 165–171, 2019.

[39] N. Luan, C. Ding, and J. Yao, “A refractive index and temperature sensor based on surface plasmon resonance in an exposed-core microstructured optical fiber,” *IEEE Photon. J.*, vol. 8, no. 2, Apr. 2016, Art. no. 4801608.

[40] I. Danlard and E. K. Akowuah, “Design and theoretical analysis of a dual-polarized quasi D-shaped plasmonic PCF microsensor for back-to-back measurement of refractive index and temperature,” *IEEE Sens. J.*, vol. 21, no. 8, pp. 9860–9868, Apr. 2021.

[41] A. Chen, Z. Yu, B. Dai, and Y. Li, “Highly sensitive detection of refractive index and temperature based on liquid-filled D-shape PCF,” *IEEE Photon. Technol. Lett.*, vol. 33, no. 11, pp. 529–532, Jun. 2021.

[42] G. Ghosh, M. Endo, and T. Iwasaki, “Temperature-dependent sellmeier coefficients and chromatic dispersions for some optical fiber glasses,” *J. Lightw. Technol.*, vol. 12, pp. 1338–1342, Aug. 1994.

[43] A. K. Sharma and B. D. Gupta, “Theoretical model of a fiber optic remote sensor based on surface plasmon resonance for temperature detection,” *Opt. Fiber Technol.*, vol. 12, pp. 87–100, 2006.

[44] D. F. Santos, A. Guerreiro, and J. M. Baptista, “Simultaneous plasmonic measurement of refractive index and temperature based on a D-type fiber sensor with gold wires,” *IEEE Sens. J.*, vol. 17, no. 8, pp. 2439–2446, Apr. 2017.

[45] S. Weng, L. Pei, C. Liu, J. Wang, J. Li, and T. Ning, “Double-side polished fiber SPR sensor for simultaneous temperature and refractive index measurement,” *IEEE Photon. Technol. Lett.*, vol. 28, no. 18, pp. 1916–1919, Sep. 2016.